Inorganic Chemistry

pubs.acs.org/IC Article

Crystal and Electronic Structures of A_2NaIO_6 Periodate Double Perovskites (A = Sr, Ca, Ba): Candidate Wasteforms for I-129 Immobilization

Sarah E. O'Sullivan, Eduardo Montoya, Shi-Kuan Sun,* Jonathan George, Cameron Kirk, Malin C. Dixon Wilkins, Philippe F. Weck, Eunja Kim,* Kevin S. Knight, and Neil C. Hyatt*

Cite This: https://dx.doi.org/10.1021/acs.inorgchem.0c03044 Read Online

ABSTRACT: The synthesis, structure, and thermal stability of the periodate double perovskites A_2NaIO_6 (A= Ba, Sr, Ca) were investigated in the context of potential application for the immobilization of radioiodine. A combination of X-ray diffraction and neutron diffraction, Raman spectroscopy, and DFT simulations were applied to determine accurate crystal structures of these compounds and understand their relative stability. The compounds were found to exhibit rock-salt ordering of Na and I on the perovskite B-site; Ba_2NaIO_6 was found to adopt the *Fm*-3*m* aristotype structure, whereas Sr_2NaIO_6 and Ca_2NaIO_6 adopt the $P2_1/n$ hettotype structure, characterized by cooperative octahedral tilting. DFT simulations determined the *Fm*-3*m* and $P2_1/n$ structures of Ba_2NaIO_6 to be energetically degenerate at room temperature, whereas diffraction and spectroscopy data evidence only the presence of the *Fm*-3*m* phase at room temperature, which may imply an incipient phase transition for this compound. The periodate double perovskites were found to exhibit remarkable thermal stability, with Ba_2NaIO_6 only decomposing above 1050 °C in air, which is apparently the highest recorded decomposition temperature so far recorded for any iodine bearing compound. As such, these compounds offer some potential for application in the immobilization of iodine-129, from nuclear fuel reprocessing, with an iodine incorporation rate of 25−40 wt%. The synthesis of these compounds, elaborated here, is also compatible with both current conventional and future advanced processes for iodine recovery from the dissolver off-gas.

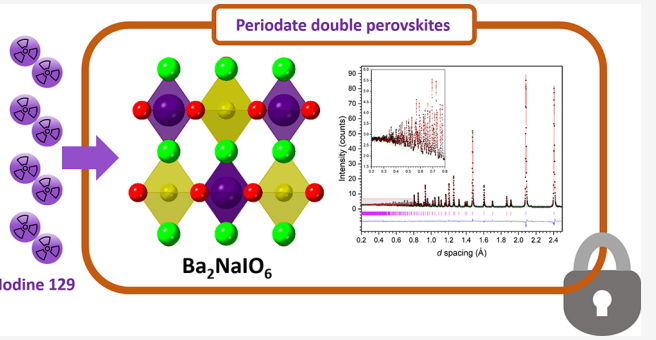

1. INTRODUCTION

The release of volatile iodine radionuclides, principally I-131 and I-129, arises from reprocessing of nuclear fuels, degradation of nuclear fuels during reactor accidents and storage, and nuclear weapons tests. I-129, with a half-life of 15.74×10^6 years, is an abundant fission product in used nuclear fuel with a fission yield of about 0.7%,[1] whereas the I-131 isotope has a half-life of 8.04 d. The iodide anion is highly soluble and weakly sorbed on mineral surfaces, over a range of geochemical conditions, and hence mobile in both environments,[2] and it is also known to bioaccumulate, being concentrated within the thyroid gland in the human body.[3] Therefore, I-129 is important as a key dose contributor in the safety case for geological disposal of radioactive wastes,[1] whereas I-131 is of critical importance for dose uptake in nuclear reactor accidents, given the *biological half-life* of 120 d.[4] I-129 is also of importance in population dose uptake in proximity to nuclear fuel reprocessing facilities; for example, data from the Savannah River site in 1989 showed that while I-129 composed only 0.00002% of the total radioactive assay released from the site, it contributed 13% of the offsite population dose.[5] The iodine biogeochemical cycle is known to be complex,[6] involving iodate (IO_3^-) and organo-iodine species, in addition to iodide (I^-), depending on the specific biogeochemical conditions, and hence there is high uncertainty in long-term predictions of iodine cycling and migration. Consequently, future regulatory practice may require immobilization and geological disposal of I-129, released from used fuel reprocessing, in contrast to the current practice of discharge and dilution in the marine environment.

A wide range of ceramic and glass wasteforms have been proposed as candidates for the immobilization and disposal of I-129, which can be categorized as follows: iodine or iodate salts (e.g., AgI or $Ba(IO_3)$[7]); tailored ceramic or glass

Received: October 13, 2020

https://dx.doi.org/10.1021/acs.inorgchem.0c03044
Inorg. Chem. XXXX, XXX, XXX−XXX

compositions incorporating iodine at the atomic scale (e.g., $Pb_5(VO_4)_3I$ ceramic or $(Ag_2O{\cdot}nB_2O_3)_{1-x}(AgI)_x$ glasses[8,9]); or composites in which a discrete iodine bearing phase is encapsulated by a metal, ceramic, or glass matrix (e.g., Al_2O_3 ceramic and silicate glass encapsulated AgI;[10,11] see Riley et al. for a comprehensive review[1]). Within these waste forms, iodine is typically incorporated as the iodide anion, which is compatible with the speciation arising from the use of a sorbent to recover iodine from the dissolver off-gas (e.g., as AgI).[1] Thermodynamic considerations suggest that solubility limited iodide wasteforms should be broadly compatible with cool, nonreducing ground waters, of low dissolved solids concentration, to avoid reductive dissolution and anion displacement reactions.[7] This would require due consideration in the site selection for a geological disposal facility or emplacement at a shallower depth. In contrast, immobilization of iodine as the iodate anion has received considerably less attention, with the exception of iodate incorporated apatite ceramics ($Ca_{10}(PO_4)_6(OH_{1.6})(IO_3)_{0.4}$) and hydrotalcite Bi–O–I phases.[12,13] Iodate incorporation within tailored wasteforms offers the advantageous compatibility with the speciation afforded by simple caustic scrubbing of the dissolver off-gas, as well as the proposed Mercurex, Iodox, and Electrolytic scrubbing processes,[1] which would enable direct iodine incorporation, without conversion to, e.g., an iodide salt. However, although iodate salts of Hg, Ba, Sr, and Ca are resistant to hydrolysis and of moderately low solubility, the solubility of the most promising candidate, $Ba(IO_3)_2$, is 5 orders of magnitude greater than AgI.[7] Additionally, iodate wasteforms are expected to be stable under relatively oxidizing conditions, and it is suggested that in the presence of reducing ground waters, wasteform dissolution could be enhanced by reduction of IO_3^- to I^-[7]. Nevertheless, it is known that IO_3^- is significantly sorbed on mineral surfaces, in contrast to I^- [14,15] (in ref 7), which, combined with isotopic dissolution and slow dissolution kinetics, may be sufficient to mitigate comparatively higher solubility.

In considering potential candidate iodate ceramic wasteforms, our attention was drawn to a family of periodate double perovskites, formulated A_2MIO_6; with reference to the ideal perovskite structure, the large (12-coordinate) A-site is occupied by A = Ba^{2+}, Sr^{2+}, Ca^{2+}, whereas the small (6 coordinate) B-site is occupied by an ordered rock-salt arrangement of I^{7+} and M^+ = Na, K, and Ag cations. The periodate double perovskites offer an iodine incorporation rate of 25–40 wt%, comparable with that demonstrated for the most efficient iodide waste form counterparts.[1] Conceptually, such a waste form would be compatible with iodine recovery processes which afford iodate speciation, from which MIO_4 (M = Na, K) is easily prepared.[16] Although periodate compounds are known to be poorly or moderately soluble, the metaperiodate Ag_5IO_6, in contrast, is known to be highly insoluble.[17−19] Periodate compounds are relatively strong oxidizing agents and hence not obviously compatible with reducing conditions of geological disposal; nevertheless, redox reactions yield the iodate species,[18] which would offer some mitigation as described above. Therefore, it was considered worthwhile to investigate the synthesis, structure, and properties of the periodate double perovskites as potential ceramic waste forms for I-129.

The first periodate double perovskites, A_2MIO_6 (A = Ba, M = Ag, Na), were reported by Sleight and Ward in 1963, formed by the solid state reaction of BaO and $NaIO_4$ at 400 °C or precipitation from a solution of $NaIO_4$ or $AgIO_4$ by addition of $Ba(OH)_2$.[20] The compounds were reported to be cubic (a = 8.4 Å) and adopted rock-salt ordering of the B-site cations. Subsequently, De Hair et al. reported the compositions A_2MIO_6 (A = Ba, M = Ag, K, Na, Li and A = Sr, M = Na), using similar methods, and reported the Raman and infrared spectra.[21] Kubel et al. reported the first crystal structure determinations for the periodate double perovskites, A_2NaIO_6 (A = Ba, Sr, Ca, Pb), in 2013, synthesized by the following: the solid state reaction between AF_2 and an excess of NaI (A = Ba, Sr, Ca); the reaction of $A(OH)_2{\cdot}8H_2O$ and $NaIO_4$ (A = Ba, Sr), at 650 °C in air; or the precipitation from a solution of nitrates with NaOH and $NaIO_4$ (A = Ba, Sr, Ca, Pb).[22] From Rietveld analysis of powder X-ray diffraction data, Ba_2NaIO_6 was reported to adopt the undistorted Fm-3m aristotype structure, whereas Sr_2NaIO_6, Ca_2NaIO_6, and Pb_2NaIO_6 were reported to adopt the $P2_1/c$ hettotype structure, with cooperative tilting of the rock-salt ordered B-site octahedra (Glazer notation, $a^+b^-b^-$).[22−24] However, our bond valence sum analysis,[25] using the reported crystal structure data, identified substantial deviations from formal valence states, as shown in Table S1, which may result from the limited accuracy and precision of locating the O positions. As highlighted by Howard et al., high resolution neutron or synchrotron X-ray diffraction data are preferable for structure determination of complex perovskites, to reveal subtle distortions of symmetry coupled with sensitivity to weak supercell reflections diagnostic of the octahedral tilt system,[24] which are not always apparent in laboratory X-ray diffraction data. Consequently, a reinvestigation of the synthesis and structure of the periodate perovskites, as reported herein, was considered a timely endeavor.

2. EXPERIMENTAL SECTION

Caution: sodium periodate, $NaIO_4$, is a strong oxidizing agent and should be handled with due caution and risk assessment.

Periodate double perovskites of general formula A_2NaIO_6 (A = Ca, Sr, Ba) were prepared by solid state synthesis. Stoichiometric quantities of the corresponding metal hydroxide ($Ca(OH)_2$, $Sr(OH)_2$, $Ba(OH)_2{\cdot}8H_2O$) and $NaIO_4$ (Sigma Aldrich, >99.8% purity) were hand ground using a pestle and mortar for 10 min under a dry nitrogen atmosphere to prevent carbonation of the hydroxide reagents. The powders were then consolidated into 10 mm pellets, pressed for 1 min under 2 tonnes pressure. The pressed pellets were packed into crucibles under a bedding of unconsolidated powder (~1 g), to prevent carbonation of the reagents during high temperature solid state reaction. All pellets were sintered in an air atmosphere muffle furnace, at 650 °C for 10 h, with a heating and cooling ramp rate of 5 °C min^{-1}. Once cooled, the pellets were recovered and gently brushed to remove any bedding material before regrinding for further analysis.

Initial X-ray diffraction (XRD) phase characterization was performed on a Bruker D2 Phaser diffractometer at room temperature in reflection mode, with Ni filtered Cu Kα radiation, λ = 1.5418 Å, and a Lynxeye position sensitive detector. High temperature X-ray diffraction (HT-XRD) was performed on a PANalytical XPert^3 diffractometer, using a parallel beam of Cu Kα radiation in reflection mode, with a PIXCel 1D position sensitive detector and Anton Parr 1200N high temperature stage. Scanning Electron Microscopy and Energy Dispersive X-ray (SEM EDX) analysis of product materials were performed using a Hitachi TM3030 SEM equipped with a Bruker Quantax 70 EDX system, operating at 15 kV and working distance of 8 mm. Specimens were prepared as a thin dusting of powder dispersed on adhesive carbon tabs. Thermogravimetric analysis mass spectrometry (TG-MS) measurements were made using a Netzsch STA 449 F3 *Jupiter* thermal analyzer coupled with a

https://dx.doi.org/10.1021/acs.inorgchem.0c03044
Inorg. Chem. XXXX, XXX, XXX−XXX

Netzsch QMS 403 *Aelos Quadro* quadrupole mass spectrometer with synthetic air carrier gas. Raman spectra were collected on a Horiba X-ploRA Plus microscope with a 532 nm laser.

Neutron diffraction data were collected from Ba_2NaIO_6, Sr_2NaIO_6, and Ca_2NaIO_6 on the POLARIS time-of-flight powder diffractometer at the ISIS pulsed spallation neutron source, Rutherford Appleton Laboratory, UK.[26,27] Ba_2NaIO_6 (3.5 g), Sr_2NaIO_6 (2.9 g), and Ca_2NaIO_6 (2.5 g) respectively were each loaded into a 6 mm diameter thin-walled vanadium sample can, which were sealed using indium wire, inside a glovebox. The sample cans were mounted on an automatic sample changer in the diffractometer and data collected for a duration of 175 μAh integrated proton beam current to the ISIS neutron target (corresponding to 1 h total neutron beam exposure) from each sample. The diffraction data were normalized to the incident beam spectrum and corrected for detector efficiency (using a vanadium standard) and sample attenuation. Data reduction and generation of files suitable for profile refinement used the Mantid open source software.[28] Structure refinement was made by Rietveld analysis of neutron diffraction data, using the GSAS and EXPGUI suite of programs[29,30] and data from the high resolution back scattering detectors (Bank 5, 2θ range 134.6−167.4°, $\Delta d/d = 3 \times 10^{-3}$[27]).

Bond valence sums (BVS) of the form $V = \Sigma e^{(r_0-r)/b}$ were calculated for each of the compounds across all cation−anion bonding pairs, using $b = 0.37$ for oxides.[25] Tabulated reference bond lengths of $r_0 = 2.285$ for Ba−O bonds, $r_0 = 2.118$ for Sr−O bonds, and $r_0 = 1.967$ for Ca−O bonds were used for the alkali earth cations.[25] For I−O bonds, $r_0 = 1.93$ was used,[31] and $r_0 = 1.661$ was used for Na−O bonds.[32] Observed bond lengths, r, were extracted from neutron refinement data. Additionally, the global instability index, $G^{II} = \left(\frac{1}{N}\sum_i d_i\right)^{0.5}$,[33] where d_i is the magnitude of difference between the BVS and the expected valence, and N is the number of atoms in the formula unit, was calculated to give the degree of failure of the BVS rule.

Density functional theory (DFT) was utilized in this study to investigate the crystal structures of the periodate double perovskites Ca_2NaIO_6, Sr_2NaIO_6, and Ba_2NaIO_6 synthesized experimentally. Total energy calculations were carried out using DFT implemented in the Vienna Ab initio Simulation Package (VASP).[34] In the Kohn−Sham (KS) equations, the interaction between valence electrons and ionic cores was described using the projector augmented wave (PAW) method[35,36] with Ca($3s^23p^64s^2$), Sr($4s^24p^65s^2$), Ba($5s^25p^66s^2$), Na($3s^1$), I($5s^25p^5$), and O($2s^22p^4$) electrons treated as valence electrons and the remaining core electrons, together with the nuclei, represented by PAW pseudopotentials. The exchange-correlation energy was calculated using the generalized gradient approximation (GGA) with the parametrization of Perdew-Burke-Ernzerhof (PBE).[37] The plane-wave energy cutoff was set to 500 eV, and a total-energy convergence criterion was fixed to 1 meV/atom. The Monkhorst-Pack scheme[38] was utilized to sample the Brillouin zone with a 3 × 3 × 3 k-point mesh. Simultaneous ionic and cell energy-relaxation calculations were carried out, without the symmetry constraint, until the Hellmann−Feynman forces acting on atoms were converged within 0.01 eV/Å.

Structures obtained from total-energy minimization with GGA/PBE were further relaxed with respect to Hellmann−Feynman forces until a convergence tolerance of 0.001 eV/Å was reached. Density functional perturbation theory (DFPT) linear response calculations were then carried out with VASP to determine the vibrational frequencies and associated intensities. The latter were computed based on the Born effective charges (BEC) tensor, which corresponds to the change in atom polarizabilities with respect to an external electric field. This computational approach was used in previous studies to successfully predict the vibrational/phonon properties of various crystalline materials.[39−41]

3. RESULTS AND DISCUSSION

3.1. Synthesis and X-ray Diffraction. The powder X-ray diffraction data of the A_2NaIO_6 periodate double perovskites synthesized by solid state reaction at 650 °C are presented in Figure 1. Analysis of these data followed the methodology

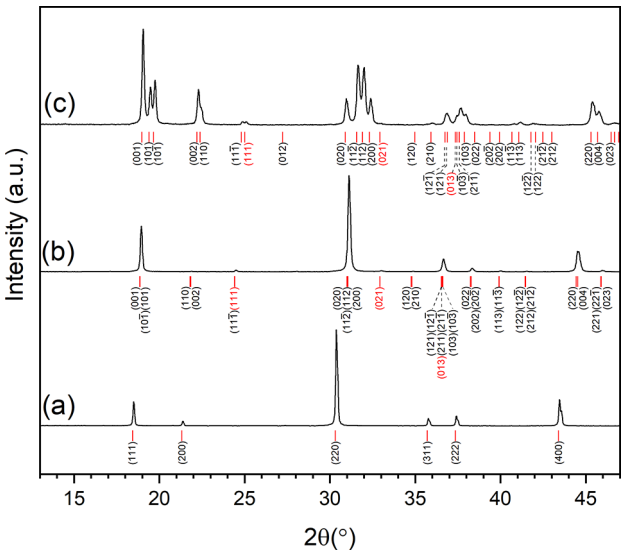

Figure 1. Indexed XRD patterns of prepared (a) Ba_2NaIO_6 (PDF 01-082-4575), (b) Sr_2NaIO_6 (PDF 04-018-9360), and (c) Ca_2NaIO_6 (PDF 04-018-9361). Tickmarks indicate allowed reflections. R-, M-, and X-point reflections are indexed in red.

recommended by Howard et al.[24] for double perovskites and demonstrated synthesis of near single phase compounds. EDX analysis of powder specimens afforded elemental compositions consistent with the target stoichiometry: $Ba_{2.05(8)}Na_{0.98(2)}I_{0.95(5)}O_6$, $Sr_{2.00(3)}Na_{0.99(3)}I_{1.02(3)}O_6$, and $Ca_{2.1(1)}Na_{1.00(3)}I_{1.1(1)}O_6$ (Note: overlap of I Lα with Ba Lα and Ca Kα emission lines afforded greater uncertainty in determination of these elements; oxygen stoichiometry was assumed given the poor precision for EDX determination). All compounds presented as creamy white powders.

The XRD pattern of Ba_2NaIO_6 was first indexed on the basis of a doubled perovskite unit cell ($a = 8$ Å), in space group Fm-$3m$. In this analysis, reflections of the type (eee) represent the fundamental reflections of the ideal cubic aristotype ABO_3 structure, in space group Pm-$3m$ (where e or o denote hkl = *even* or *odd*, respectively). Rock-salt ordering of cations on the B-site gives rise to R-point reflections indexed as (ooo), which were clearly observed as a result of the high contrast in X-ray scattering factors of Na and I (in the language of group theory, this ordering corresponds to a symmetry breaking mode described by the irreducible representation R^+_1). Antiphase (−) tilting of B-site octahedra, i.e., rotation of the opposite sense in successive layers, also makes a small contribution to the intensity of R-point reflections (irreducible representation R^+_4), but this is masked by the dominant contribution of B-site ordering. Antiphase octahedral tilting would necessarily further lower the symmetry, resulting in obvious splitting of fundamental reflections, which was not observed. No additional reflections could be indexed, which implied an absence of in-phase octahedral tilting, although such reflections would be expected to be relatively weak in X-ray diffraction, due to the relatively small scattering factor of O. From this analysis, we deduce Ba_2NaIO_6 to be a rock-salt ordered double perovskite, adopting space group Fm-$3m$ with the Glazer tilt system $a^0a^0a^0$.

https://dx.doi.org/10.1021/acs.inorgchem.0c03044
Inorg. Chem. XXXX, XXX, XXX−XXX

Table 1. Ba_2NaIO_6 Structural Parameters Determined from Rietveld Analysis of Neutron Diffraction Data

space group: *Fm*-3*m*, Z = 4, a = 8.3335(2) Å, V = 578.731(4) Å^3					
formula weight: 520.542 u					
atom	site	x	y	z	U_{iso} × 100 (Å^2)
Ba	8c	0.25	0.25	0.25	0.497(8)
I	4a	0	0	0	0.14(1)
Na	4b	0.5	0.5	0.5	1.27(3)
O1	24e	0.22420(3)	0	0	0.937(6)
powder statistics:	χ^2 = 3.966	R_{wp} = 3.02%	R_p = 4.18%		

Considering Ca_2NaIO_6, reflections indexed as (400) and (220) in the *Fm*-3*m* cell were observed to be split and (with others) could be indexed on the basis of monoclinic symmetry (respectively, (220) (004) in intensity ratio 2:1 and (020) (112) (11-2) (200) in intensity ratio 1:2:2:1). Further inspection identified both M-point reflections of the type (*eoo*) diagnostic of in-phase (+) octahedral tilting (irreducible representation M^+_3), e.g., (013), and R-point reflections that are primarily a signature of B-site cation ordering, e.g., (111). Coupling of the B-site cation ordering and antiphase octahedral tilting (R-point reflections) and in-phase octahedral tilting (M-point reflections) is expected to afford additional X-point reflections, of the type (*eeo*), which were also apparent, e.g., (021). From this analysis, we deduce Ca_2NaIO_6 to be a double rock-salt ordered perovskite phase, adopting space group $P2_1/n$ with the Glazer tilt system $a^-a^-c^+$. This systematic analysis validates the previous assignment of space group $P2_1/c$ ($a^+b^-b^-$) which is the standard setting of $P2_1/n$; the latter is preferred in the perovskite literature, since it approximates an orthogonal cell with $\beta \approx 90°$.

The XRD data of Sr_2NaIO_6 also presented reflection profiles and splitting of fundamental reflections diagnostic of monoclinic symmetry. Additionally, R-point and X-point reflections (e.g., (111) and (021), respectively) were evident; however, reflection overlap did not allow unambiguous identification of the M-point reflections (e.g., (013)). Note, however, such reflections are implicit, since the associated in-phase octahedral tilting, coupled with rock-salt ordering and antiphase octahedral tilting, affords significant intensity at the X-point reflections, which are clearly observed. These observations are sufficient to deduce that Sr_2NaIO_6 is a rock-salt ordered double perovskite phase, isostructural with Ca_2NaIO_6, adopting space group $P2_1/n$ with the Glazer tilt system $a^-a^-c^+$; this systematic analysis validates the previous assignment of the standard setting $P2_1/c$ ($a^+b^-b^-$).

3.2. Structure Refinement. Rietveld analysis of neutron powder diffraction data utilized an initial double perovskite model in *Fm*-3*m* or $P2_1/n$, according to prior analysis of X-ray powder diffraction data. Initial inspection of data identified diagnostic R-, M-, and X-point reflections, in agreement with analysis of powder X-ray diffraction data. The background was fitted using a fifth order shifted Chebyshev polynomial function, followed by systematic refinement of lattice structural parameters, and profile parameters. Rock-salt ordering of Na and I was initially assumed; in the final stage of the refinement, the potential for antisite disorder was examined but found to be insignificant, by refinement under constraint of full site occupancy. Additional reflections were observed in the data of Ca_2NaIO_6, which could not be indexed in space group $P2_1/n$, which were attributed to unidentified impurities.

3.2.1. Structure Refinement of Ba_2NaIO_6. Structure refinement converged rapidly to a satisfactory fit with χ^2 = 2.49, R_{wp} = 2.40%, and R_p = 4.05%, for 17 variables including 6 structural parameters. The final structural parameters are summarized in Table 1, a schematic representation of the crystal structure is shown in Figure 2, and the profile fit is shown in Figure 3. The determined key bond lengths and bond valence sums are summarized in Table 2.

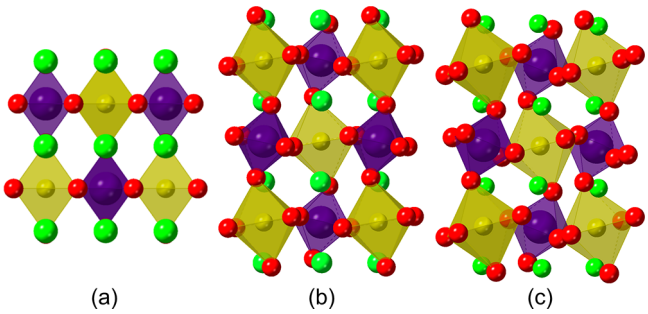

Figure 2. Structures of A_2NaIO_6 compounds modeled from neutron diffraction data. a) Ba_2NaIO_6 viewed down [110], and b) Sr_2NaIO_6 and c) Ca_2NaIO_6 viewed down [010]. Green spheres indicate respective alkali earth cations (Ba, Sr, or Ca), yellow octahedra indicate sodium cations, purple octahedra indicate iodine cations, and red spheres indicate oxygen anions.

The crystal structure of Ba_2NaIO_6 was thus determined to adopt cubic *Fm*-3*m* symmetry (tilt system $a^0a^0a^0$). Ba is 12-fold

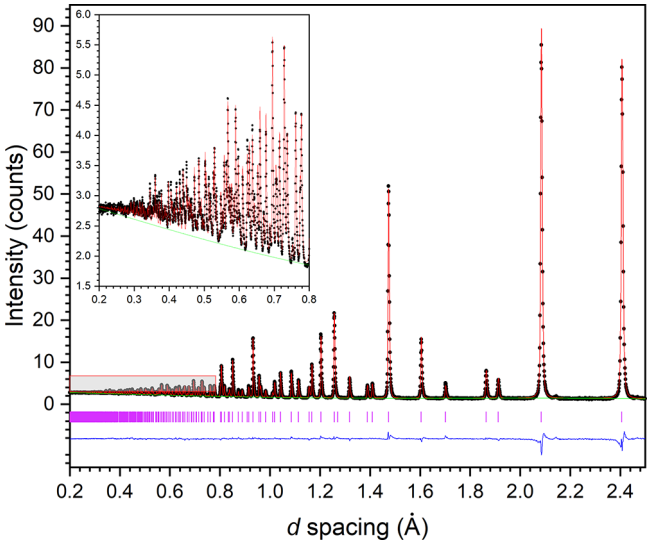

Figure 3. Rietveld refinement fit (red line) of powder neutron diffraction data (black dots) for Ba_2NaIO_6. Purple tick marks indicate allowed reflections in the *Fm*-3*m* space group. The blue line indicates difference profile.

https://dx.doi.org/10.1021/acs.inorgchem.0c03044
Inorg. Chem. XXXX, XXX, XXX−XXX

Table 2. Bond Lengths and Calculated Bond Valence Sums for A_2NaIO_6 Perovskites

Ba_2NaIO_6			Sr_2NaIO_6			Ca_2NaIO_6		
bond	length (Å)	BVS	bond	length (Å)	BVS	bond	length (Å)	BVS
Ba−O1 (x12)	2.95420(2)	1.97	Sr−O1	3.186(2)	1.89	Ca−O1	3.617(2)	1.95
			Sr−O1	2.658(2)		Ca−O1	2.375(2)	
			Sr−O1	2.550(3)		Ca−O1	2.340(3)	
			Sr−O1	3.248(3)		Ca−O1	3.364(3)	
			Sr−O2	2.571(4)		Ca−O2	2.381(3)	
			Sr−O2	2.790(3)		Ca−O2	2.683(3)	
			Sr−O2	2.875(3)		Ca−O2	2.725(3)	
			Sr−O2	3.366(4)		Ca−O2	3.654(2)	
			Sr−O3	2.819(3)		Ca−O3	2.574(2)	
			Sr−O3	2.556(4)		Ca−O3	2.366(2)	
			Sr−O3	3.398(3)		Ca−O3	3.671(3)	
			Sr−O3	2.846(3)		Ca−O3	2.961(3)	
I−O1 (x6)	1.8684(3)	7.09	I−O1 (x2)	1.863(2)	7.08	I−O1 (x2)	1.861(2)	7.12
			I−O2 (x2)	1.870(2)		I−O2 (x2)	1.865(2)	
			I−O3 (x2)	1.874(2)		I−O3 (x2)	1.874(2)	
Na−O1 (x6)	2.2984(3)	1.07	Na−O1 (x2)	2.281(2)	1.12	Na−O1 (x2)	2.341(2)	0.98
			Na−O2 (x2)	2.275(2)		Na−O2 (x2)	2.297(2)	
			Na−O3 (x2)	2.286(2)		Na−O3 (x2)	2.368(2)	

Table 3. Sr_2NaIO_6 Structural Parameters Determined from Rietveld Analysis of Neutron Diffraction Data

space group: $P2_1/n$, $Z = 2$, $a = 5.7591\ (2)$ Å, $b = 5.7673(1)$ Å, $c = 8.1341(2)$ Å, $\beta = 89.934(3)°$, $V = 270.172(4)$ Å^3					
formula weight: 421.128 u					
atom	site	x	y	z	$U_{iso} \times 100$ (Å^2)
Na	2a	0	0	0	1.08(4)
I	2b	0	0	0.5	0.24(1)
Sr	4e	0.0057(3)	0.5287(2)	0.2499(3)	0.83(1)
O1	4e	−0.0665(4)	−0.0177(3)	0.2762(2)	0.72(2)
O2	4e	0.2433(4)	0.3071(4)	0.0331(3)	1.12(3)
O3	4e	0.3124(4)	0.7608(4)	0.0355(3)	1.24(3)
powder statistics:	$\chi^2 = 2.561$	$R_{wp} = 2.26\%$	$R_p = 3.05\%$		

coordinated by oxygen at the center of the cuboctahedral cavity defined by eight corner-sharing BO_6 octahedra, occupied alternately by Na and I. The Na and I cations are fully ordered in a rock-salt arrangement on the B site, as expected from the large difference in charge and ionic radius which affords a substantial contribution to the total Madelung energy, as shown by Rosenstein and Schor (i.e., the electrostatic contribution to the lattice energy).[42] The compound is thus isostructural with Ba_2NaBO_6 double perovskites, with an identical charge difference of six units between B and B′ cations (B = Re, Os).[43,44]

The Goldschmidt tolerance factor,[45] t, provides a metric by which to assess bond length mismatch and potential for structural distortion, with respect to the cubic aristotype structure. For double perovskites, t is expressed as

$$t = \frac{r_A + r_O}{\sqrt{2}(r_B + r_O)} \quad (1)$$

where r_A, r_B, and r_O denote the oxidation state and coordination specific (mean) ionic radii determined by Shannon and Prewitt[46] of the A and B cations and O anions. The tolerance factor, $t = 0.98$, within the stability field of $0.98 < t < 1.01$ was typically observed for adoption of the undistorted $Fm\text{-}3m$ structure.[47] Bond valence sums are commensurate with the expected valence of each of the cations, and the global instability index $G_{II} = 0.06$ v.u., indicating a stable structure.[33]

3.2.2. Structure Refinement of Sr_2NaIO_6. Structure refinement converged rapidly to an excellent fit with $\chi^2 = 2.26$, $R_{wp} = 2.55\%$, and $R_p = 3.05\%$, for 36 variables including 22 structural parameters. The final structural parameters are summarized in Table 3, the profile fit is shown in Figure 4, and a schematic representation of the crystal structure is shown in Figure 2. The determined key bond lengths and bond valence sums are summarized in Table 2. The crystal structure of Sr_2NaIO_6 was thus determined to adopt monoclinic $P2_1/n$ symmetry (tilt system $a^-a^-c^+$), with cooperative antiphase and in-phase tilting of slightly distorted BO_6 octahedra, occupied alternately by Na and I in a fully ordered rock-salt arrangement. Consequently, Sr adopts a distorted 12-fold coordination environment with 8 short and 4 long Sr−O bonds. As indicated by the Glazer tilt system, the NaO_6 and IO_6 octahedra show an in-phase tilt and an antiphase tilt. These were calculated using the mode decomposition formulism demonstrated for similar elpasolite structures, yielding an in-phase tilt of 7.8° about [001] and an antiphase tilt of 10.9° about [110].[48] Sr_2NaIO_6 is thus isostructural with the double perovskite Sr_2NaReO_6, although the Re counterpart exhibited considerable disorder of the oxygen sublattice which was not observed here.[44] The tolerance factor of Sr_2NaIO_6, $t = 0.92$, is outside the stability field of $0.98 < t < 1.01$ typically observed for adoption of the undistorted $Fm\text{-}3m$ structure[47] but within the range observed

https://dx.doi.org/10.1021/acs.inorgchem.0c03044
Inorg. Chem. XXXX, XXX, XXX−XXX

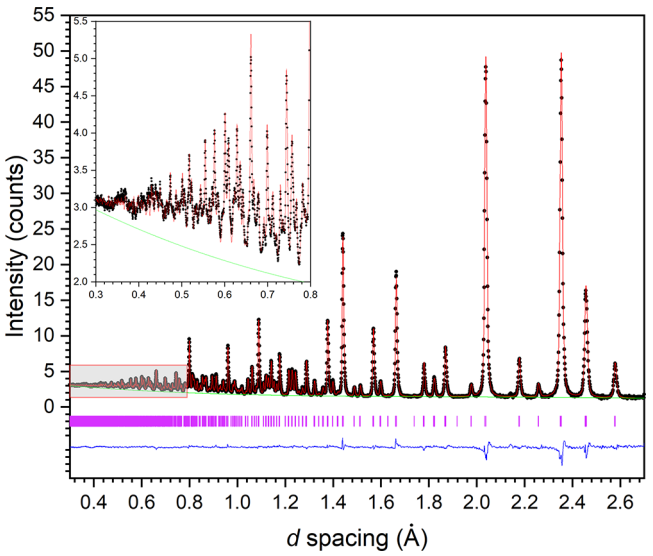

Figure 4. Rietveld refinement fit (red line) of powder neutron diffraction data (black dots) for Sr_2NaIO_6. Purple tick marks indicate allowed reflections in the $P2_1/n$ space group. The blue line indicates difference profile.

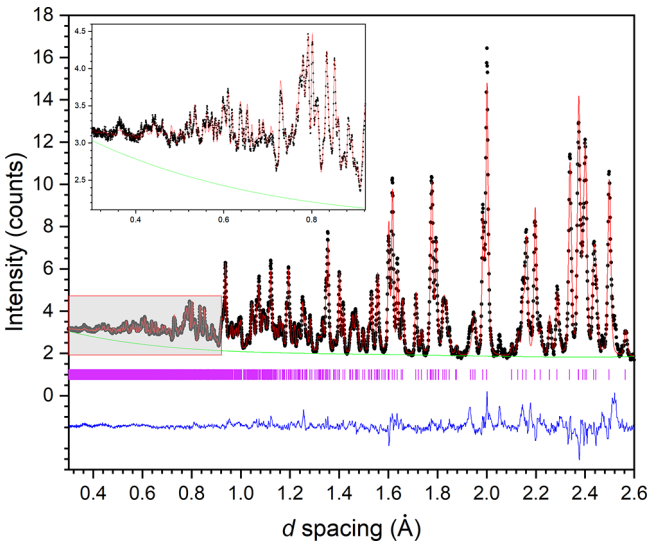

Figure 5. Rietveld refinement fit (red line) of powder neutron diffraction data (black dots) for Ca_2NaIO_6. Purple tick marks indicate allowed reflections in the $P2_1/n$ space group. The blue line indicates difference profile.

for isostructural $P2_1/n$ perovskites, $0.83 < t < 0.98$.[47] The Sr cation is evidently too small for the 12 coordinate cuboctahedral site, resulting in cooperative octahedral tilting as a result of bond length mismatch. Bond valence sums show the Sr cation to be underbonded, which is presumably a consequence of maintaining adequate Na−O and I−O bond lengths, while minimizing bond length mismatch. This is compensated by significant overbonding of the Na ion, although I ions remain within the acceptable tolerance of ±5% around the expected valence. The calculated global instability index arising from the BVS is G_{II} = 0.09 which is approaching the steric strain region $0.1 < G_{II} < 0.2$ v.u.; however, it still indicates a stable structure.[33]

3.2.3. Structure Refinement of Ca_2NaIO_6. Structure refinement converged rapidly to an excellent fit with χ^2 = 3.38, R_{wp} = 2.53%, and R_p = 4.27%, for 34 variables including 22 structural parameters. The final structural parameters are summarized in Table 4, the profile fit is shown in Figure 5, and a schematic representation of the crystal structure is shown in Figure 2. The determined key bond lengths and bond valence sums are summarized in Table 2.

The crystal structure of Ca_2NaIO_6 was determined to be isostructural with Sr_2NaIO_6 adopting monoclinic $P2_1/n$ symmetry (tilt system $a^-a^-c^+$). The Ca site adopts a similarly distorted 12-fold coordination environment with 8 short and 4 long Ca−O bonds, arising from cooperative antiphase and in-phase tilting of slightly distorted BO_6 octahedra. Na and I adopt a fully ordered rock-salt arrangement in the B sites; the NaO_6 and IO_6 octahedra show an in-phase tilt angle of 11.7° about [001] and an antiphase tilt angle of 17.8° about [110].[48] The greater extent of octahedra tilting in comparison to Sr_2NaIO_6 arises due to the greater bond length mismatch. The tolerance factor of Ca_2NaIO_6, t = 0.89, is within the range $0.83 < t < 0.98$ observed for isostructural $P2_1/n$ perovskites. The low tolerance factor of Ca_2NaIO_6 implies considerable bond length mismatch and hence structural strain, since the Ca cation is too small for the 12 coordinate cuboctahedral site, resulting in cooperative octahedral tilting. Bond valence sums show the Ca cation to be slightly underbonded, which is presumably a consequence of maintaining adequate Na−O and I−O bond lengths. The global instability index is G_{II} = 0.07 v.u. indicating a stable and well determined structure.[33]

3.3. DFT Studies. Total energy curves of each periodate double perovskite structure are provided in Figure 6, for model structures crystallizing in the cubic $Fm\text{-}3m$ and monoclinic $P2_1/n$ space groups. For both Ca_2NaIO_6 and Sr_2NaIO_6, the monoclinic phase was determined to be energetically favorable compared to the cubic phase, in agreement with diffraction and Raman spectroscopy data. The cubic and monoclinic structures of Sr_2NaIO_6 resulted in a relatively small difference

Table 4. Ca_2NaIO_6 Structural Parameters Determined from Rietveld Analysis of Neutron Diffraction Data

space group: $P2_1/n$, Z = 2, a = 5.5365(1) Å, b = 5.7845(1) Å, c = 7.9352(2) Å, β = 90.834(2)°, V = 254.103(8) Å^3					
formula weight: 326.044 u					
atom	site	x	y	z	$U_{iso} \times 100$ (Å^2)
Na	2a	0	0	0	0.62(5)
I	2b	0	0	0.5	0.041(9)
Ca	4e	0.0160(3)	0.5575(3)	0.2447(3)	0.68(3)
O1	4e	−0.1108(3)	−0.0537(3)	0.2809(2)	0.64(2)
O2	4e	0.2243(3)	0.3266(3)	0.0453(2)	0.79(2)
O3	4e	0.3381(3)	0.7666(3)	0.0705(2)	0.71(2)
powder statistics:	χ^2 = 3.381	R_{wp} = 2.53%	R_p = 4.27%		

https://dx.doi.org/10.1021/acs.inorgchem.0c03044
Inorg. Chem. XXXX, XXX, XXX−XXX

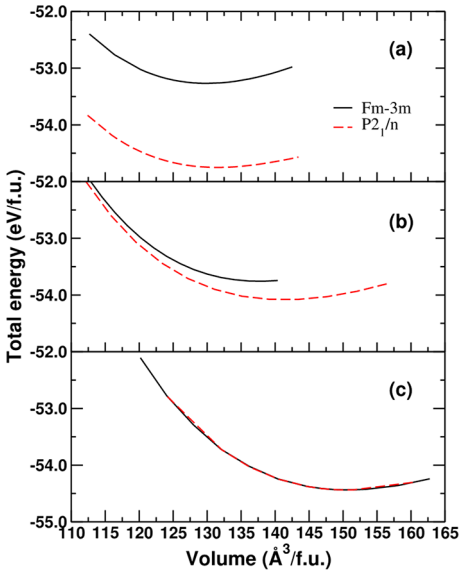

Figure 6. Total energy curves of (a) Ca_2NaIO_6, (b) Sr_2NaIO_6, and (c) Ba_2NaIO_6 as functions of volume per formula unit (f.u.) calculated at the GGA/PBE level of theory for structures crystallizing in the cubic *Fm*-3*m* (solid black curves) and monoclinic $P2_1/n$ (dashed red curves) space groups.

in energetics, compared to Ca_2NaIO_6. The cubic phase is slightly less energetically favorable by 0.3 eV/f.u. in Sr_2NaIO_6 and 1.4 eV/f.u. in Ca_2NaIO_6. For Ba_2NaIO_6, the monoclinic $P2_1/n$ and cubic *Fm*-3*m* structures were determined to be energetically degenerate. This suggests that a mixture of phases could coexist at room temperature or the presence of an incipient phase transition. Analysis of neutron diffraction data did not identify reflection asymmetry, weak supercell reflections, or unusual thermal parameters characteristic of a lower symmetry structure. Likewise, analysis of the Raman spectrum Ba_2NaIO_6 was consistent with *Fm*-3*m* symmetry. Future work will examine the possibility of a *Fm*-3*m* to $P2_1/n$ phase transition in Ba_2NaIO_6 at low temperature.

The formation energies of Ca_2NaIO_6 ($P2_1/n$), Sr_2NaIO_6 ($P2_1/n$), and Ba_2NaIO_6 (*Fm*-3*m*) were calculated using eqs 2 and 3:

$$2M(OH)_2 + NaIO_4 \rightarrow M_2NaIO_6 + 2H_2O \quad (2)$$

$$E_f = [E(M_2NaIO_6) + E(2H_2O)] - [E(2M(OH)_2) + E(NaIO_4)] \quad (3)$$

The former describes the synthesis of the periodate double perovskites as applied in this study (where M = Ca, Sr, or Ba), while the latter is the formation energy (E_f) for that reaction. The calculated formation energies of Ca_2NaIO_6 ($P2_1/n$), Sr_2NaIO_6 ($P2_1/n$), and Ba_2NaIO_6 (*Fm*-3*m*) were 5.518, 5.060, and 4.157 eV/f.u., respectively. Ba_2NaIO_6 has the lowest formation energy, followed by Sr_2NaIO_6 and Ca_2NaIO_6. A similar trend can be seen in the total energy difference between the cubic *Fm*-3*m* and monoclinic $P2_1/n$ phases, which is the largest in Ca_2NaIO_6, followed by Sr_2NaIO_6 and the smallest in Ba_2NaIO_6.

The calculated lattice parameters of Ca_2NaIO_6 ($P2_1/n$), Sr_2NaIO_6 ($P2_1/n$), and Ba_2NaIO_6 (*Fm*-3*m*) are in excellent agreement with the experimentally determined values, as summarized in Table 5, with optimized structures also presented in Figure S1. Accordingly, the simulated XRD patterns from the DFT optimized structures, shown in Figure S2, match the experimentally determined patterns. The monoclinic $P2_1/n$ and cubic *Fm*-3*m* structures for Ba_2NaIO_6 exhibit nearly identical XRD patterns; the converged atomic positions in the former structure are not significantly different from those in the latter.

Computed bond lengths and atomic positions are given in Tables S2 and S3, respectively, and show a good agreement with the experimentally derived values, across all three compositions. For Ca_2NaIO_6, bond lengths of Ca−O*X*, I−O*X*, and Na−O*X* (*X* = 1,2,3) are overestimated by 0.006 to 0.060 Å, the slight overestimation characteristic of the use of GGA functionals. The calculated bond lengths of Sr_2NaIO_6 are in very close agreement with the experimental measurements, with differences typically smaller than 0.001 Å. For example, the calculated bond lengths for Sr−O1 are 2.553, 2.658, 3.186, and 3.248 Å in excellent agreement with the experimentally derived values of 2.550, 3.248, 3.186, and 3.248 Å, respectively.

The atomic positions in the Ba_2NaIO_6 *Fm*-3*m* phase (Table S3) are essentially identical to the experimentally determined Rietveld refinement data, with a small difference of 0.002 Å for the *x* position of O1. The lattice constants are overestimated by about 0.1 Å. The bond lengths reported for the crystal appear to be in good agreement with the experimental results, albeit slightly overestimated for the Ba−O1 and I−O1 bonds. Na−O1 share similar values between the DFT and experimental values due to the effective DFT representation of the highly electropositive sodium core and its interaction with electronegative oxygens. Since no experimental data for the hypothetical $P2_1/n$ Ba_2NaIO_6 crystal are available, only the DFT bond lengths are reported in Table S3. The Ba−O*X* bond lengths in the $P2_1/n$ phase are predicted to differ by up to 0.01 Å. The bond lengths of I−O*X* in both phases are nearly identical, yet there is a relatively small difference of 0.008 Å between the Na−O*X* bonds.

3.4. Raman Spectra. Raman spectra were simulated using DFPT linear response calculations to obtain vibrational

Table 5. Calculated Lattice Parameters and Unit Cell Volumes of Ca_2NaIO_6, Sr_2NaIO_6, and Ba_2NaIO_6[a]

	Ba_2NaIO_6		Ba_2NaIO_6		Sr_2NaIO_6		Ca_2NaIO_6	
space group	*Fm*-3*m*, *Z* = 4		$P2_1/n$, *Z* = 2		$P2_1/n$, *Z* = 2		$P2_1/n$, *Z* = 2	
	DFT	exp	DFT	exp	DFT	exp	DFT	exp
a (Å)	8.444	8.3335	8.445		5.836	5.7591	5.575	5.5365
b (Å)			5.971		5.949	5.7673	5.844	5.7845
c (Å)			5.973		8.259	8.1341	8.046	7.9352
β (°)	90	90	89.97		90.06	89.93	91.03	90.83
V (Å^3)	602.090	578.731	301.358		286.708	270.172	261.752	254.103

[a]Experimental data from this study are also reported for comparison.

https://dx.doi.org/10.1021/acs.inorgchem.0c03044
Inorg. Chem. XXXX, XXX, XXX−XXX

frequencies. These were assumed to have a natural line broadening of Lorentzian shape with FWHM of 5 cm^{-1}. These data were combined with experimental measurements in Figure 7, with Raman active frequencies and mode assignments

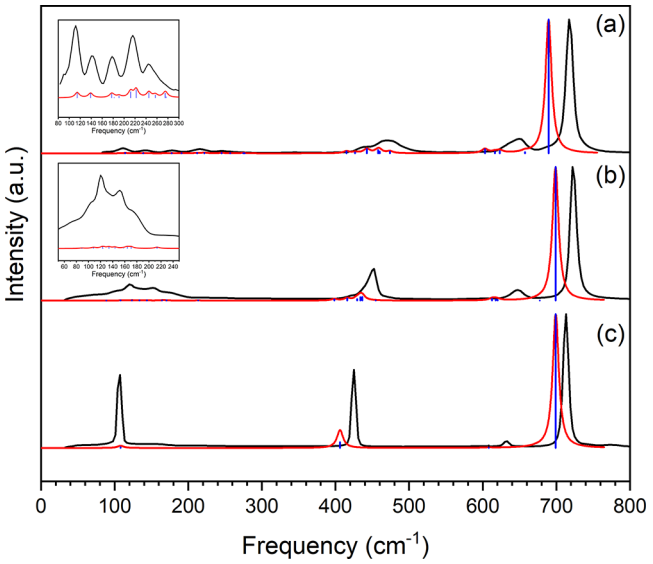

Figure 7. Raman spectra of (a) Ca_2NaIO_6 ($P2_1/n$), (b) Sr_2NaIO_6 ($P2_1/n$), and (c) Ba_2NaIO_6 (Fm-3m) simulated from DFPT at the GGA/PBE level (blue), with experimental measurement (black). Natural line broadening was simulated from DFPT eigenfrequencies using a Lorentzian line shape function with a full width at half-maximum (FWHM) of 5 cm^{-1} (red). Insets show the detail of low frequency regions for Ca_2NaIO_6 and Sr_2NaIO_6.

given in Table 6. The modeled and experimental data are self-consistent within systematic calibration error and are consistent with those spectra previously reported.[22]

With N = 20 atoms (Z = 2) per monoclinic $P2_1/n$ cell, Ca_2NaIO_6 and Sr_2NaIO_6 possess 3N = 60 degrees of freedom. Among these modes of vibration of the C_{2h} point group,[49] there are three acoustic modes: $\Gamma_{acoustic}(3) = A_u + 2B_u$, which corresponds to zero-frequency modes of translation at the Γ-point, i.e., one longitudinal acoustic mode associated with the A_u irreducible representation (irrep), and two transverse acoustic modes with B_u irrep. The remaining 57 optical modes can be represented as $\Gamma_{optical}(57) = 12A_g + 17A_u + 12B_g + 16B_u$, where vibrational modes belonging to the A_g, A_u, B_g, and B_u irreps are nondegenerate.

According to selection rules for the C_{2h} point group, only the 24 optical modes belonging to the *gerade* (g) irreps, i.e., $12A_g + 12B_g$, are Raman active, while all 33 optical modes belonging to the *ungerade* (u) irreps, i.e., $17A_u + 16B_u$, are infrared (IR) active. However, coupling of the A_g and B_g modes typically occurs in $P2_1/n$ perovskite, thus significantly reducing the number of bands observed in Raman spectra. The 24 Raman-active modes can be decomposed as

$$\Gamma = 6T(3A_g + 3B_g) + 6L(3A_g + 3B_g) + 6\nu_5(3A_g + 3B_g) + 4\nu_2(2A_g + 2B_g) + 2\nu_1(A_g + B_g)$$

where low-intensity translational (T) lattice vibrational modes of Ca/Sr (4e sites) are usually observed in the region 80−240 cm^{-1}, low-intensity libration (L) lattice modes of Ca/Sr and internal oxygen bending modes (ν_5) of IO_6 octahedra appear

Table 6. Raman-Active Frequencies (in cm^{-1}) and Mode Assignment of Ca_2NaIO_6 and Sr_2NaIO_6 ($P2_1/n$) and Ba_2NaIO_6 (Fm-3m) Simulated from DFPT at the GGA/PBE Level, along with Raman Band Centers Measured in This Study

	Ca_2NaIO_6		Sr_2NaIO_6		Ba_2NaIO_6	
assign.	DFPT	exp	DFPT	exp	DFPT	exp
ν_1	689.7	717	698.9	722	699.2	713
ν_1	689.4		695.7			
ν_2	657.3	650	677.5	647	608.2	633
ν_2	623.3		620.3			
ν_2	616.5		617.6			
ν_2	603.0		612.7			
ν_5	473.8	472	454.6	452	406.2	425
ν_5	460.1	437	436.5			
ν_5	457.7		433.8			
ν_5	442.6		429.5			
ν_5	426.7		415.9			
ν_5	415.0		398.3			
L	276.7	246	213.4	175	108.1	107
L	274.9	216	170.5	152		
L	256.9		164.1			
L	245.2		158.0			
L	222.0		143.8			
L	211.9		133.8			
T	190.8	177	230.1	175		
T	181.9	143	124.1	152		
T	177.4	111	123.4	120		
T	138.9		108.2			
T	114.4		93.9			
T	114.2		88.9			

in the ranges 100−280 cm^{-1} and 390−480 cm^{-1}, respectively, and broad low-intensity asymmetric oxygen stretches (ν_2) and intense symmetric oxygen stretches (ν_1) of IO_6 octahedra are present in the regions 600−680 cm^{-1} and 680−950 cm^{-1}, respectively.

The cubic Fm-3m unit cell of Ba_2NaIO_6 is composed of 40 atoms (Z = 4), resulting in 120 in degrees of freedom. The vibration analysis was carried out using the corresponding 10-atom primitive cell (Z = 1). In the O_h point group,[49] the acoustic modes, $\Gamma_{acoustic}(3) = 3T_{1u}$, belong to the triply degenerate T_{1u} irrep, while the remaining 27 optical modes can be represented as $\Gamma_{optical}(27) = A_{1g} + E_g + T_{2u} + 2T_{2g} + 4T_{1u} + T_{1g}$, where vibrational modes of the A_{1g}, E_g, and T irreps are nondegenerate, doubly degenerate, and triply degenerate, respectively. Among optical modes, 12 modes belonging to the T_{1u} irrep are IR active. The 9 Raman-active modes belong to the $\Gamma = A_{1g} + E_g + 2T_{2g}$ irreps, which can be decomposed alternatively as $\Gamma = L(T_{2g}) + \nu_5(T_{2g}) + \nu_2(E_g) + \nu_1(A_{1g})$, where ν_5, ν_2, and ν_1 have a similar meaning as in the $P2_1/n$ case, while L corresponds here to libration lattice modes of IO_6 octahedra. For perovskites crystallizing in the Fm-3m space group, libration lattice modes L of IO_6 octahedra typically appear in the 100−300 cm^{-1} range, the ν_5 mode from the oxygen bending motion in octahedra occurs in the 300−450 cm^{-1} range, and the strong ν_1 oxygen symmetric stretch in octahedra is usually seen in the region 650−900 cm^{-1}. The ν_2 asymmetric oxygen stretch band at a slightly lower frequency is either very weak or even nonexistent in high-symmetry Fm-3m perovskites and appears as a much narrower peak compared to $P2_1/n$ perovskites.

https://dx.doi.org/10.1021/acs.inorgchem.0c03044
Inorg. Chem. XXXX, XXX, XXX−XXX

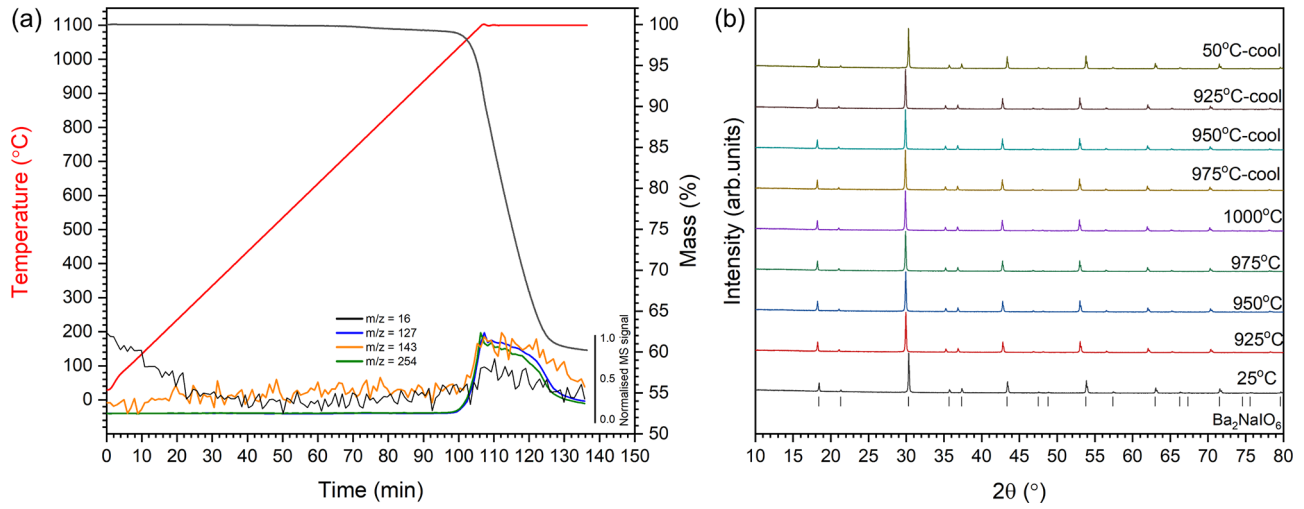

Figure 8. High temperature data for Ba_2NaIO_6. a) TGA-MS measurement with normalized m/z channels. b) HT-PXRD data for ramp to 1000 °C and subsequent cool. Tickmarks indicate allowed reflections.

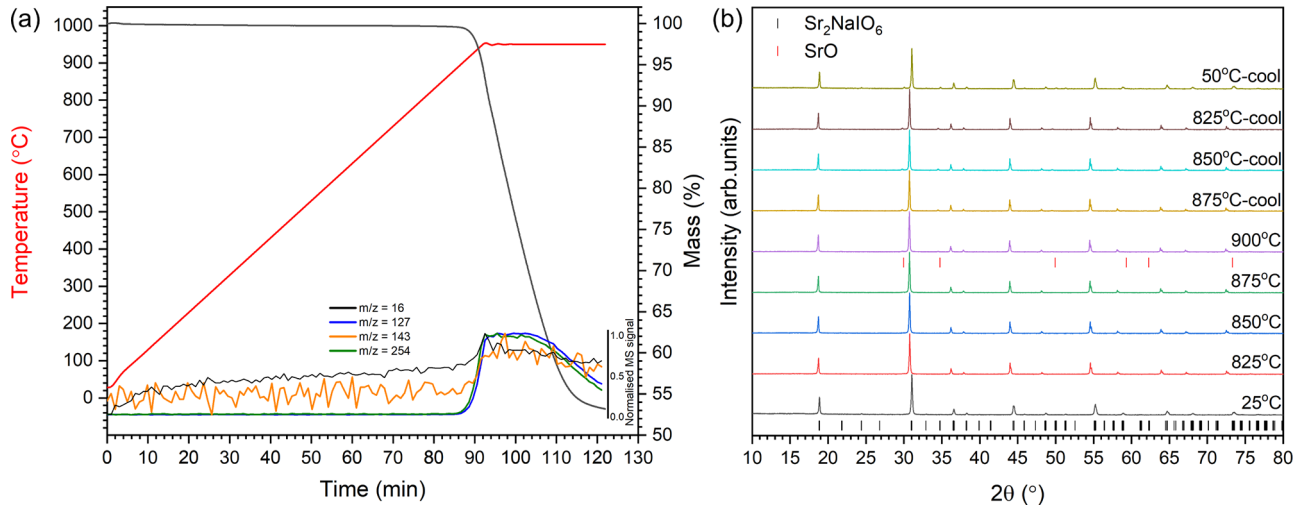

Figure 9. High temperature data for Sr_2NaIO_6. a) TGA-MS measurement with normalized m/z channels. b) HT-PXRD data for ramp to 900 °C and subsequent cool. Black tickmarks indicate allowed reflections for Sr_2NaIO_6, and red tickmarks indicate the onset of allowed reflections for SrO.

3.5. High Temperature Behavior. The high temperature behavior of the periodate double perovskites was investigated by in situ high temperature X-ray powder diffraction (HT-PXRD) and thermogravimetric analysis (TGA-MS) coupled with mass spectroscopy.

TGA-MS analysis of Ba_2NaIO_6 (Figure 8) revealed this compound to remain stable up to a remarkably high temperature of 1050 °C, above which a sharp weight loss was observed. This was accompanied by signals at m/z = 127 and 254 (attributed to I^+ and I_2^+, respectively) and weaker signals at m/z = 16 and 143 (attributed to O_2^+ and IO^+). The final weight loss was determined to be 39.77 wt%, in good agreement with the expected weight loss of 41.1 wt% for the following decomposition reaction:

$$Ba_2NaIO_6(s) = 2BaO(s) + NaI(g) + 2O_2(g) \quad (4)$$

The sample was recovered from the TGA-MS analysis and confirmed to comprise BaO by XRD. Additionally, the material was characterized by SEM-EDX analysis (Figure S3) which evidenced the complete loss of NaI from the material, according to the absence of Na Kα and I Lα emission, consistent with the above decomposition reaction and XRD analysis. An additional strong signal arising from Al Kα emission was also evident, attributed to reaction between BaO and the Al_2O_3 crucible used for the measurement. Additionally, SEM images showed clear evidence for growth in particle size and development of faceting for the residual BaO which may be a result of a fluxing effect of NaI assisting diffusion (and reaction with the Al_2O_3 crucible). No MS signal was apparent at expected m/z = 23 or 150, attributable to Na or NaI, respectively, below or above 1050 °C. The melting point of NaI is 661 °C,[50] and therefore, it undoubtedly plated out in the gas transfer line between TGA and MS, which was maintained at 500 °C. The decomposition temperature of Ba_2NaIO_6 is higher than that reported for any periodate or metaperiodate reported in the most comprehensive tabulation available;[51] hitherto, the compound reported to have the highest thermal stability was $Ba_5(IO_6)_2$, which decomposes above 950 °C.

The high temperature behavior of Ba_2NaIO_6 was also investigated by in situ HT-PXRD but limited to a temperature of 1000 °C, as shown in Figure 8. The HT-PXRD data could

https://dx.doi.org/10.1021/acs.inorgchem.0c03044
Inorg. Chem. XXXX, XXX, XXX−XXX

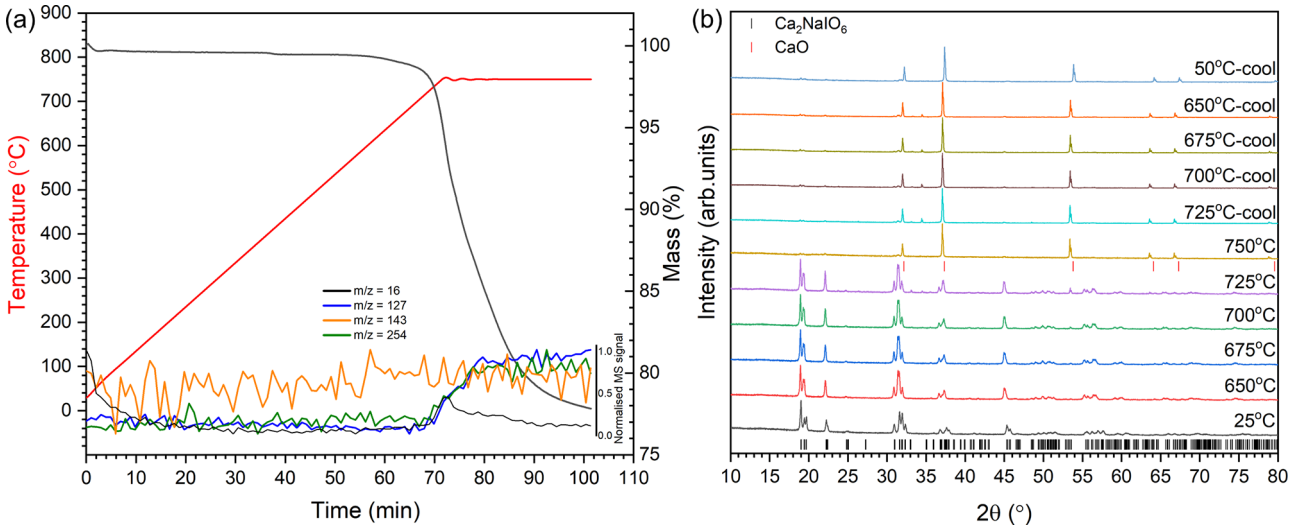

Figure 10. High temperature data for Ca_2NaIO_6. a) TGA-MS measurement with normalized m/z channels. b) HT-PXRD data for ramp to 750 °C and subsequent cool. Black tickmarks indicate allowed reflections for Ca_2NaIO_6, and red tickmarks indicate the onset of allowed reflections for CaO.

be indexed fully on the *Fm*-3*m* structure of Ba_2NaIO_6, up to 1000 °C, and on subsequent cooling to 50 °C, demonstrating the thermal stability of the compound within this temperature window, consistent with TG-MS data. In particular, the R-point reflections, diagnostic of rock-salt ordering of Na and I on the B-site, remained clearly observable throughout. Thus, no order−disorder transition involving Na and I cations on the B-site is apparent up to 1000 °C.

TGA-MS analysis of Sr_2NaIO_6 (Figure 9) revealed this compound to remain stable up to 950 °C, accompanied by strong MS signals at m/z = 127 and 254 and weaker signals for m/z = 16 and 143, as observed for the Ba counterpart. The final weight loss was determined to be 46.8 wt%, in good agreement with the expected weight loss of 50.79 wt% for the following decomposition reaction:

$$Sr_2NaIO_{6(s)} = 2SrO_{(s)} + NaI_{(g)} + 2O_{2(g)} \quad (5)$$

The material recovered from TGA-MS analysis was characterized by SEM-EDX analysis (Figure S4) which showed the complete loss of NaI, and XRD analysis revealed the product to be SrO, in agreement with the above mechanism. SEM imaging showed evidence for some growth in particle size and development of faceting for the residual SrO, though to a less extent than observed in the case of Ba_2NaIO_6, likely due to reduced kinetics of diffusion at the lower temperature at which NaI is evolved.

Further investigation of the high temperature behavior of Sr_2NaIO_6 was made by *in situ* HT-PXRD, up to 900 °C, as shown in Figure 9. The HT-PXRD data could be indexed throughout with the $P2_1/n$ Sr_2NaIO_6 structure, with a secondary phase of SrO at 900 °C evident. R-point reflections indicative of rock-salt ordering on the B-site coupled with antiphase octahedral tilting (e.g., (111)) and X-point reflections (e.g., (021)) arising from the coupling of the aforementioned R- and implied M-point reflections were observed only in the room temperature and 50 °C data sets, prior to and after the heating regimen. Therefore, a reversible phase transition, involving relaxation of the coupled octahedral tilts, may occur between room temperature and 825 °C, though this must be understood as a tentative interpretation, given the weak nature of such reflections, and further investigation is warranted.

Finally, TGA-MS analysis of Ca_2NaIO_6 (Figure 10) revealed this compound to remain stable up to 730 °C, accompanied by MS signals at m/z = 127 and 254, as observed for the Ba and Sr counterparts. Unlike Ba and Sr, a stronger signal corresponding to m/z = 16 is seen and is not coupled to m/z = 143, which is not apparent in these data. The final weight loss obtained at 730 °C was determined to be 21.79 wt%; however, phase analysis of the post TGA product revealed this to be a mixture of majority CaO and residual Ca_2NaIO_6 and thus represents only a partial decomposition at 730 °C. Expected weight loss is 65.6 wt% for the following overall decomposition reaction:

$$Ca_2NaIO_{6(s)} = 2CaO_{(s)} + NaI_{(g)} + 2O_{2(g)} \quad (6)$$

The material recovered from TGA-MS analysis after ramping to 750 °C was characterized by SEM-EDX analysis (Figure S5) which showed the complete loss of I but some retention of Na, and XRD analysis revealed the product to be CaO together with an unidentified impurity phase. SEM imaging showed evidence for some evidence for sintering of the residual material but not the growth in particle size and development of faceting observed in the case of Ba_2NaIO_6 and Sr_2NaIO_6. These data suggest that thermal decomposition of Ca_2NaIO_6 proceeds via a different mechanism, compared to the Ba and Sr counterparts, involving the sequential loss of O_2 and I followed by volatilization of Na_2O.

Figure 11 shows the formation energy (E_f) and decomposition temperature of the A_2NaIO_6 compounds, as a function of the Goldschmidt tolerance factor, *t*. Ba_2NaIO_6 is the most thermally stable compound when heated in air, showing the onset of decomposition at 1050 °C, followed by Sr_2NaIO_6 at 950 °C and Ca_2NaIO_6 at 730 °C. As expected, this is inversely correlated to the formation energies previously discussed, which established Ba_2NaIO_6 to have the lowest formation energy at 4.517 eV/f.u., followed by Sr_2NaIO_6 at 5.060 eV/f.u. and Ca_2NaIO_6 at 5.518 eV/f.u. The formation energy indicates the thermodynamic driver for compound synthesis and, therefore, a comparatively large and positive E_f is

https://dx.doi.org/10.1021/acs.inorgchem.0c03044
Inorg. Chem. XXXX, XXX, XXX−XXX

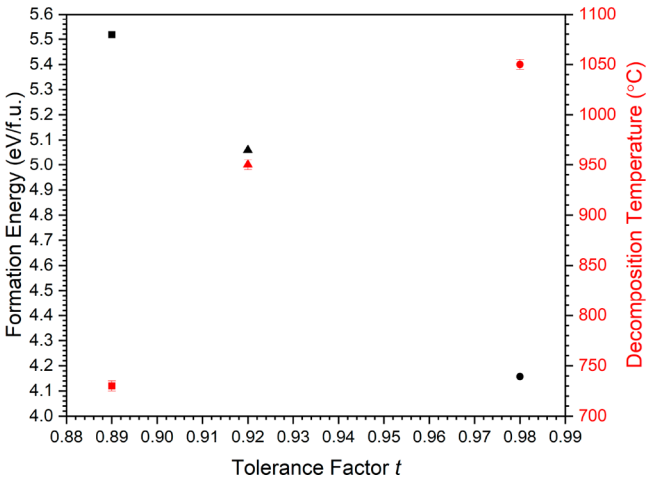

Figure 11. Formation energy and decomposition temperature as a function of tolerance factor for Ba_2NaIO_6 (circles), Sr_2NaIO_6 (triangles), and Ca_2NaIO_6(squares). Formation energies are plotted in black, and decomposition temperatures are plotted in red.

correlated with lower decomposition temperature. This can be further correlated with the structural stability of the compounds expressed as the tolerance factor. Ba_2NaIO_6, with a tolerance factor of $t = 0.98$, was shown to be an undistorted cubic *Fm*-3*m* symmetry, while the lower tolerance factors of the $P2_1/n$ compounds, $t \ll 1$, indicate bond length mismatch giving rise to structural distortion. For Ca_2NaIO_6, the tolerance factor is close to the lower limit observed for double perovskites with the tilt system $a^-a^-c^+$ ($P2_1/n$), $0.83 < t < 0.98$,[47] suggesting this compound is at the limit of structural stability; it therefore has the lowest decomposition temperature and highest formation energy, E_f.

4. CONCLUSIONS

The A_2NaIO_6 (A = Ba, Sr, Ca) double perovskite structures were determined from a combination of powder neutron and X-ray diffraction data, Raman spectroscopy, and DFT calculations. These perovskites are characterized by rock-salt ordering of I and Na on the B-site; Ba_2NaIO_6 adopts the *Fm*-3*m* aristotype structure without cooperative octahedral tilting, whereas Sr_2NaIO_6 and Ca_2NaIO_6 adopt the $P2_1/n$ hettotype structure with cooperative antiphase and in-phase octahedral tilting consistent with expectations of group theory. DFT calculations established the $P2_1/n$ structure to be energetically favorable, compared to *Fm*-3*m*, for Ca_2NaIO_6 and Sr_2NaIO_6, consistent with experimental data. In contrast, DFT calculations determined the $P2_1/n$ and *Fm*-3*m* structures of Ba_2NaIO_6 to be energetically degenerate, whereas diffraction and Raman spectroscopy data establish the structure to be cubic at room temperature. This may point to an incipient low temperature phase transition in Ba_2NaIO_6 involving the onset of cooperative octahedral tilting.

Ba_2NaIO_6 was found to exhibit remarkable thermal stability, decomposing only above 1050 °C (in air), and as far as we are able to ascertain, this compound exhibits the highest thermal stability of any iodine bearing substance so far documented. The decomposition temperatures of the A_2NaIO_6 perovskites follow the trend of formation energy determined from DFT, A = Ba > Sr > Ca, with Sr_2NaIO_6 decomposing above 950 °C and Ca_2NaIO_6 above 730 °C (in air). Ba_2NaIO_6 and Sr_2NaIO_6 thermal decompose by evaporation of NaI, whereas thermal decomposition of Ca_2NaIO_6 proceeds by loss of O_2 and I_2, followed by evaporation of Na_2O.

With regard to application of A_2NaIO_6 perovskites as an immobilization matrix for radioiodine, this investigation has demonstrated considerable potential. These compounds offer an iodine incorporation rate of 25−40 wt%, comparable with that demonstrated for the most efficient iodide waste form counterparts. The synthesis of A_2NaIO_6 phases is achieved in a quantitative yield, by reaction between $A(OH)_2{\cdot}nH_2O$ and $NaIO_4$, in one step at a relatively low temperature of 650 °C. This approach is compatible with conventional caustic and other advanced scrubbing processes for fuel dissolver off-gas which afford radioiodine speciated as iodate, which can easily be converted to $NaIO_4$. Thermal stability in the context of fire scenarios is one criterion of interest for selection of a waste immobilization matrix, and in this regard, Ba_2NaIO_6 surpasses the performance of alternate ceramic options. Future work will investigate the potential for forming sintered ceramic bodies of the periodate perovskites to facilitate examination of their dissolution behavior.

■ ASSOCIATED CONTENT

Supporting Information

The Supporting Information is available free of charge at https://pubs.acs.org/doi/10.1021/acs.inorgchem.0c03044.

Comparison of BVS between this work and previous work, structures representation from DFT-optimization, simulated X-ray diffraction patterns, bond lengths and atomic positions comparison between DFT and experimental data, and SEM-EDS analysis of A_2NaIO_6 powder pre- and post-HT-XRD (PDF)

Accession Codes

CCDC 2036872−2036874 contains the supplementary crystallographic data for this structure. These data can be obtained free of charge via www.ccdc.cam.ac.uk/data_request/cif, or by emailing data_request@ccdc.cam.ac.uk, or by contacting The Cambridge Crystallographic Data Centre, 12 Union Road, Cambridge CB2 1EZ, UK; fax: +44 1223 336033.

■ AUTHOR INFORMATION

Corresponding Authors

Shi-Kuan Sun − *Department of Materials Science and Engineering, University of Sheffield, Sheffield S1 3JD, U.K.*; orcid.org/0000-0002-1688-5072; Email: shikuan.sun@sheffield.ac.uk

Eunja Kim − *Department of Physics and Astronomy, University of Nevada, Las Vegas, Nevada 89154, United States*; Email: kimej@physics.unlv.edu

Neil C. Hyatt − *Department of Materials Science and Engineering, University of Sheffield, Sheffield S1 3JD, U.K.*; orcid.org/0000-0002-2491-3897; Email: n.c.hyatt@sheffield.ac.uk

Authors

Sarah E. O'Sullivan − *Department of Materials Science and Engineering, University of Sheffield, Sheffield S1 3JD, U.K.*

Eduardo Montoya − *Department of Chemistry and Biochemistry, University of Nevada, Las Vegas, Nevada 89154, United States*

Jonathan George − *Department of Chemistry and Biochemistry, University of Nevada, Las Vegas, Nevada 89154, United States*

https://dx.doi.org/10.1021/acs.inorgchem.0c03044
Inorg. Chem. XXXX, XXX, XXX−XXX

Cameron Kirk − *Department of Electrical and Computer Engineering, University of Nevada, Las Vegas, Nevada 89154, United States*

Malin C. Dixon Wilkins − *Department of Materials Science and Engineering, University of Sheffield, Sheffield S1 3JD, U.K.;* orcid.org/0000-0003-1520-7672

Philippe F. Weck − *Sandia National Laboratories, Albuquerque, New Mexico 87185, United States;* orcid.org/0000-0002-7610-2893

Kevin S. Knight − *Department of Materials Science and Engineering, University of Sheffield, Sheffield S1 3JD, U.K.; Department of Earth Sciences, University College London, London WC1E 6BT, U.K.*

Complete contact information is available at: https://pubs.acs.org/10.1021/acs.inorgchem.0c03044

Notes

The views expressed in the article do not necessarily represent the views of the U.S. DOE or the United States Government. The authors declare no competing financial interest.

■ ACKNOWLEDGMENTS

Components of this research utilized the HADES/MIDAS facility at the University of Sheffield established with financial support from EPSRC and BEIS, under grant EP/T011424/1.[52] Experiments at the ISIS Neutron and Muon Source were supported by a beamtime allocation RB1920341 from the Science and Technology Facilities Council; we thank Dr. R. Smith for assistance with data acquisition.[26] S.O.S., S.K.S., and N.C.H. are grateful for financial support from EPSRC under grant numbers EP/L015390/1 and EP/S01019X/1. Components of this research was performed using funding received from the U.S. Department of Energy, Office of Nuclear Energy's Nuclear Energy University Program (NEUP). Sandia National Laboratories is a multimission laboratory managed and operated by National Technology and Engineering Solutions of Sandia, LLC., a wholly owned subsidiary of Honeywell International, Inc., for the U.S. Department of Energy's (DOE) National Nuclear Security Administration under contract DE-NA0003525. This work was performed, in part, at the Center for Integrated Nanotechnologies, an Office of Science User Facility operated for the U.S. Department of Energy (DOE) Office of Science.

■ REFERENCES

(1) Riley, B. J.; Vienna, J. D.; Strachan, D. M.; McCloy, J. S.; Jerden, J. L. Materials and Processes for the Effective Capture and Immobilization of Radioiodine: A Review. *J. Nucl. Mater.* **2016**, *470*, 307−326.

(2) Yeager, C. M.; Amachi, S.; Grandbois, R.; Kaplan, D. I.; Xu, C.; Schwehr, K. A.; Santschi, P. H. Microbial Transformation of Iodine: From Radioisotopes to Iodine Deficiency. *Adv. Appl. Microbiol.* **2017**, *101*, 83−136.

(3) Kaplan, D. I.; Denham, M. E.; Zhang, S.; Yeager, C.; Xu, C.; Schwehr, K. A.; Li, H. P.; Ho, Y. F.; Wellman, D.; Santschi, P. H. Radioiodine Biogeochemistry and Prevalence in Groundwater. *Crit. Rev. Environ. Sci. Technol.* **2014**, *44* (20), 2287−2335.

(4) Thomas, G. Radiation and Thyroid Cancer-an Overview. *Radiat. Prot. Dosim.* **2018**, *182* (1), 53−57.

(5) Kantelo, M. V.; Bauer, L. R.; Marter, W. L.; Murphy, J. C. E.; Zeigler, C. C. *Radioiodine in the Savannah River Site Environment*; Report WSRC-RP-90-424-2; Westinghouse Savannah River Co.: United States, 1993; DOI: 10.2172/10122501.

(6) Santschi, P. H.; Xu, C.; Zhang, S.; Schwehr, K. A.; Grandbois, R.; Kaplan, D. I.; Yeager, C. M. Iodine and Plutonium Association with Natural Organic Matter: A Review of Recent Advances. *Appl. Geochem.* **2017**, *85*, 121−127.

(7) Taylor, P. *A Review of Methods for Immobilizing Iodine-129 Arising from a Nuclear Fuel Recycle Plant, with Emphasis on Waste-Form Chemistry*; Canada, 1990.

(8) Dalba, G.; Fornasini, P.; Rocca, F. Short Range Order in AgI:Ag2O:B2O3 Glasses: Results from Exafs and Related Techniques. *J. Non-Cryst. Solids* **1990**, *123* (1), 310−314.

(9) Stennett, M. C.; Pinnock, I. J.; Hyatt, N. C. Rapid Synthesis of $Pb_5(VO_4)_3I$, for the Immobilisation of Iodine Radioisotopes, by Microwave Dielectric Heating. *J. Nucl. Mater.* **2011**, *414* (3), 352−359.

(10) Tanabe, H.; Sakuragi, T.; Yamaguchi, K.; Sato, T.; Owada, H. Development of New Waste Forms to Immobilize Iodine-129 Released from a Spent Fuel Reprocessing Plant. *Adv. Sci. Technol.* **2010**, *73*, 158−170.

(11) Garino, T. J.; Nenoff, T. M.; Krumhansl, J. L.; Rademacher, D. X. Low-Temperature Sintering Bi-Si-Zn-Oxide Glasses for Use in Either Glass Composite Materials or Core/Shell ^{129}I Waste Forms. *J. Am. Ceram. Soc.* **2011**, *94* (8), 2412−2419.

(12) Krumhansl, J. L.; Nenoff, T. M. Hydrotalcite-Like Layered Bismuth-Iodine-Oxides as Waste Forms. *Appl. Geochem.* **2011**, *26* (1), 57−64.

(13) Campayo, L.; Grandjean, A.; Coulon, A.; Delorme, R.; Vantelon, D.; Laurencin, D. Incorporation of Iodates into Hydroxyapatites: A New Approach for the Confinement of Radioactive Iodine. *J. Mater. Chem.* **2011**, *21* (44), 17609−17611.

(14) Couture, R. A.; Seitz, M. G. Sorption of Anions of Iodine by Iron Oxides and Kaolinite. *Nucl. Chem. Waste Manage.* **1983**, *4* (4), 301−306.

(15) Machesky, M. L.; Bischoff, B. L.; Anderson, M. A. Calorimetric Investigation of Anion Adsorption onto Goethite. *Environ. Sci. Technol.* **1989**, *23* (5), 580−587.

(16) Hill, A. E. Ternary Systems. VII. The Periodates of the Alkali Metals. *J. Am. Chem. Soc.* **1928**, *50* (10), 2678−2692.

(17) Thompson, N. R. In *The Chemistry of Copper, Silver and Gold*; Massey, A. G., Thompson, N. R., Johnson, B. F. G., Davis, R., Eds.; Pergamon: Oxford, UK, 1973; Chapter 28, pp 79−128, DOI: 10.1016/B978-0-08-018860-7.50007-4.

(18) Reimer, I.; Lister, M. W. The Compounds $KMnO_6$ and $NaMnIO_6$. *Can. J. Chem.* **1961**, *39* (12), 2431−2435.

(19) Levason, W. The Coordination Chemistry of Periodate and Tellurate Ligands. *Coord. Chem. Rev.* **1997**, *161*, 33−79.

(20) Sleight, A. W.; Ward, R. Compounds of Post-Transition Elements with the Ordered Perovskite Structure. *Inorg. Chem.* **1964**, *3* (2), 292−292.

(21) De Hair, J. T. W.; Corsmit, A. F.; Blasse, G. Vibrational Spectra and Force Constants of Periodates with Ordered Perovskite Structure. *J. Inorg. Nucl. Chem.* **1974**, *36* (2), 313−315.

(22) Kubel, F.; Wandl, N.; Pantazi, M.; D'Anna, V.; Hagemann, H. The Periodate-Based Double Perovskites M_2NaIO_6 (M = Ca, Sr, and Ba). *Z. Anorg. Allg. Chem.* **2013**, *639* (6), 892−898.

(23) Kubel, F.; Pantazi, M.; Wandl, N.; Hagemann, H. Synthesis and Crystal Structures of a Stable, a Metastable and a High Temperature Modification of Pb_2NaIO_6. *Z. Anorg. Allg. Chem.* **2014**, *640* (15), 3184−3189.

(24) Howard, C. J.; Kennedy, B. J.; Woodward, P. M. Ordered Double Perovskites - a Group-theoretical Analysis. *Acta Crystallogr., Sect. B: Struct. Sci.* **2003**, *59* (4), 463−471.

(25) Brown, I. D.; Altermatt, D. Bond-Valence Parameters Obtained from a Systematic Analysis of the Inorganic Crystal Structure Database. *Acta Crystallogr., Sect. B: Struct. Sci.* **1985**, *41* (4), 244−247.

(26) Hyatt, N. Crystal Structure of Ba_2NaIO_6, Sr_2NaIO_6m and Ca_2NaIO_6 *STFC ISIS Neutron and Muon Source* 2019; DOI: 10.5286/ISIS.E.RB1990180-1, DOI: 10.5286/ISIS.E.RB1990181-1, and DOI: 10.5286/ISIS.E.RB1990182-1.

(27) Smith, R. I.; Hull, S.; Tucker, M. G.; Playford, H. Y.; McPhail, D. J.; Waller, S. P.; Norberg, S. T. The Upgraded Polaris Powder Diffractometer at the Isis Neutron Source. *Rev. Sci. Instrum.* **2019**, *90* (11), 115101.
(28) Arnold, O.; Bilheux, J. C.; Borreguero, J. M.; Buts, A.; Campbell, S. I.; Chapon, L.; Doucet, M.; Draper, N.; Ferraz Leal, R.; Gigg, M. A.; Lynch, V. E.; Markvardsen, A.; Mikkelson, D. J.; Mikkelson, R. L.; Miller, R.; Palmen, K.; Parker, P.; Passos, G.; Perring, T. G.; Peterson, P. F.; Ren, S.; Reuter, M. A.; Savici, A. T.; Taylor, J. W.; Taylor, R. J.; Tolchenov, R.; Zhou, W.; Zikovsky, J. Mantid—Data Analysis and Visualization Package for Neutron Scattering and M Sr Experiments. *Nucl. Instrum. Methods Phys. Res., Sect. A* **2014**, *764*, 156−166.
(29) Larson, A. C.; Von Dreele, R. B. *General Structure Analysis System (GSAS)*; Los Alamos National Laboratory Report LAUR 86-748, United States, 2004.
(30) Toby, B. Expgui, a Graphical User Interface for GSAS. *J. Appl. Crystallogr.* **2001**, *34* (2), 210−213.
(31) Brese, N. E.; O'Keeffe, M. Bond-Valence Parameters for Solids. *Acta Crystallogr., Sect. B: Struct. Sci.* **1991**, *47* (2), 192−197.
(32) Allmann, R. Beziehungen Zwischen Bindungslängen Und Bindungsstärken in Oxidstrukturen. *Monatsh. Chem.* **1975**, *106* (3), 779−793.
(33) Brown, I. D. Recent Developments in the Methods and Applications of the Bond Valence Model. *Chem. Rev.* **2009**, *109* (12), 6858−6919.
(34) Kresse, G.; Furthmüller, J. Efficient Iterative Schemes for ab initio Total-Energy Calculations Using a Plane-Wave Basis Set. *Phys. Rev. B: Condens. Matter Mater. Phys.* **1996**, *54* (16), 11169−11186.
(35) Blöchl, P. E. Projector Augmented-Wave Method. *Phys. Rev. B: Condens. Matter Mater. Phys.* **1994**, *50* (24), 17953−17979.
(36) Kresse, G.; Joubert, D. From Ultrasoft Pseudopotentials to the Projector Augmented-Wave Method. *Phys. Rev. B: Condens. Matter Mater. Phys.* **1999**, *59* (3), 1758−1775.
(37) Perdew, J. P.; Burke, K.; Ernzerhof, M. Generalized Gradient Approximation Made Simple. *Phys. Rev. Lett.* **1996**, *77* (18), 3865−3868.
(38) Monkhorst, H. J.; Pack, J. D. Special Points for Brillouin-Zone Integrations. *Phys. Rev. B.* **1976**, *13* (12), 5188−5192.
(39) Weck, P. F.; Kim, E.; Buck, E. C. On the Mechanical Stability of Uranyl Peroxide Hydrates: Implications for Nuclear Fuel Degradation. *RSC Adv.* **2015**, *5* (96), 79090−79097.
(40) Weck, P. F.; Kim, E.; Jové-Colón, C. F. Relationship between Crystal Structure and Thermo-Mechanical Properties of Kaolinite Clay: Beyond Standard Density Functional Theory. *Dalton Trans.* **2015**, *44* (28), 12550−12560.
(41) Weck, P. F.; Kim, E. Thermodynamics of Technetium: Reconciling Theory and Experiment Using Density Functional Perturbation Analysis. *Dalton Trans.* **2015**, *44* (28), 12735−12742.
(42) Rosenstein, R. D.; Schor, R. Superlattice Madelung Energy of Idealized Ordered Cubic Perovskites. *J. Chem. Phys.* **1963**, *38* (7), 1789−1790.
(43) Stitzer, K. E.; Smith, M. D.; Zur Loye, H.-C. Crystal Growth of Ba_2MoSO_6 (M = Li, Na) from Reactive Hydroxide Fluxes. *Solid State Sci.* **2002**, *4* (3), 311−316.
(44) Bharathy, M.; Zur Loye, H. C. Crystal Growth and Structural Investigation of A_2BReO_6 (a = Sr, Ba; B = Li, Na). *J. Solid State Chem.* **2008**, *181* (10), 2789−2795.
(45) Goldschmidt, V. Geochemische verteilungsgesetze der elemente. *Skrifter der Norske Videnskaps-Akad* **1926**, *8* (3), 529−533.
(46) Shannon, R. D.; Prewitt, C. T. Effective Ionic Radii in Oxides and Fluorides. *Acta Crystallogr., Sect. B: Struct. Crystallogr. Cryst. Chem.* **1969**, *25* (5), 925−946.
(47) Lufaso, M. W.; Barnes, P. W.; Woodward, P. M. Structure Prediction of Ordered and Disordered Multiple Octahedral Cation Perovskites Using Spuds. *Acta Crystallogr., Sect. B: Struct. Sci.* **2006**, *62* (3), 397−410.
(48) Knight, K. S. Parameterization of Centrosymmetric Elpasolite-Type Crystal Structures in terms of Symmetry-Adapted Basis-Vectors of the Primitive Cubic Aristotype Phase. *Can. Mineral.* **2009**, *47* (2), 401−420.
(49) Dresselhaus, M. S.; Dresselhaus, G.; Jorio, A. *Group Theory*; Springer Berlin Heidelberg: Berlin, Heidelberg, 2008; DOI: 10.1007/978-3-540-32899-5.
(50) Galamba, N.; Costa Cabral, B. J. First Principles Molecular Dynamics of Molten NaI: Structure, Self-Diffusion, Polarization Effects, and Charge Transfer. *J. Chem. Phys.* **2007**, *127* (9), 094506.
(51) Stern, K. *High Temperature Properties and Thermal Decomposition of Inorganic Salts with Oxyanions*; Taylor & Francis: Boca Raton, FL, 2000; DOI: 10.1201/9781420042344.
(52) Hyatt, N. C.; Corkhill, C. L.; Stennett, M. C.; Hand, R. J.; Gardner, L. J.; Thorpe, C. L. The Hades Facility for High Activity Decommissioning Engineering & Science: Part of the UK National Nuclear User Facility. *IOP Conf. Ser.: Mater. Sci. Eng.* **2020**, *818*, 012022.

https://dx.doi.org/10.1021/acs.inorgchem.0c03044
Inorg. Chem. XXXX, XXX, XXX−XXX